

AC Josephson effect in a gate-tunable Cd_3As_2 nanowire superconducting weak link

R. Haller,^{1,*} M. Osterwalder,¹ G. Fülöp,^{1,2} J. Ridderbos,³ M. Jung,⁴ and C. Schönenberger^{1,5,†}

¹*Department of Physics, University of Basel, Klingelbergstrasse 82 CH-4056, Switzerland*

²*Department of Physics, Institute of Physics, Budapest University of Technology and Economics and*

MTA-BME Nanoelectronics Momentum Research Group, Műegyetem rkp. 3., H-1111 Budapest, Hungary

³*MESA+ Institute for Nanotechnology, University of Twente, P.O. Box 217, 7500 AE Enschede, Netherlands*

⁴*DGIST Research Institute, DGIST, Daegu 42988, Republic of Korea*

⁵*Swiss Nanoscience Institute, University of Basel, Klingelbergstrasse 82 CH-4056, Switzerland*

(Dated: June 1, 2023)

Three-dimensional topological Dirac semimetals have recently gained significant attention, since they possess exotic quantum states. When constructing Josephson junctions utilizing these materials as the weak link, the fractional ac Josephson effect emerges in the presence of a topological supercurrent contribution. We investigate the ac Josephson effect in a Dirac semimetal Cd_3As_2 nanowire using two complementary methods: by probing the radiation spectrum and by measuring Shapiro patterns. With both techniques, we find that conventional supercurrent dominates at all investigated doping levels and that any potentially present topological contribution falls below our detection threshold. The inclusion of thermal noise in a resistively and capacitively shunted junction (RCSJ) model allows us to reproduce the microwave characteristics of the junction. With this refinement, we explain how weak superconducting features can be masked and provide a framework to account for elevated electronic temperatures present in realistic experimental scenarios.

I. INTRODUCTION

Topological superconductivity is a hot topic in condensed matter physics, since the quasi-particle excitations that govern its attributes, so-called Majorana fermions, follow non-Abelian exchange statistics – a property that could revolutionize quantum computation, as it allows the implementation of fault-tolerant operations [1–7]. While theoretical concepts on those exotic particles have already been developed in the past decades [8–12], platforms to synthesize Majoranas are still being established and clear experimental evidence of their existence is lacking [13].

We employ Dirac semimetal Cd_3As_2 nanowire Josephson junctions as a platform for the search of topological superconductivity. Dirac semimetals possess exotic electronic properties emerging from three dimensional Dirac cones - crossings between valence and conduction bands with linear dispersion relations [14–19]. They host topological surface states [20] and develop Majorana flat bands in Josephson junctions [21]. Recently, the superconducting proximity effect has been observed in Cd_3As_2 nanowires and nanoplates, including Josephson supercurrent carried by surface states [22]. In this context, π - and 4π -periodic supercurrent states, and topological supercurrent oscillations have been reported [23, 24].

In our Cd_3As_2 nanowire junctions, we hunt for signatures of the fractional ac Josephson effect arising from 4π -periodic contributions in the current-phase relation (CPR) that are a direct consequence of topologically protected Andreev bound states, i.e., Majorana modes [8, 25, 26]. To this end, we investigate the ac

Josephson effect by two complementary methods: (i) via the detection of Josephson radiation and (ii) by measuring Shapiro steps.

In the latter experiment, missing odd Shapiro steps are the fingerprint of topological supercurrent admixtures [27–29]. This effect has been observed for different material platforms: InSb nanowire junctions exposed to in-plane magnetic fields [30], Bi_xSe_y -based [31–33] and HgTe-based [34, 35] topological insulator junctions, Bi_xSb_y Dirac semimetal nanoplate junctions [36], $(\text{Bi}_{1-x}\text{Sb}_x)_2\text{Te}_3$ -based topological insulator nanowire junctions [37] and includes Cd_3As_2 nanowire junctions [24].

When measuring Josephson radiation, the signature of a topologically non-trivial supercurrent is the halving of the fundamental Josephson frequency $f_J = q^*V/h$, with q^* being the effective charge, V the dc voltage bias and h the Planck constant. This occurs since the topological supercurrent is carried by single electrons ($q^* = e$) instead of Cooper-pairs in the case of conventional junctions ($q^* = 2e$) [25]. Evidence for topological emission has only been claimed from a gate-tunable Al-HgTe-Al topological insulator junction [38] and on an Al-InAs-Al nanowire junction exposed to in-plane magnetic fields [39].

The (fractional) ac Josephson effect principally distinguishes conventional from topological junctions, but many experimental aspects pose a challenge to unambiguously prove the emergence of Majorana states such as: marginal 4π -supercurrent contributions, elevated electronic temperatures, environmental circuit effects [40, 41], Landau-Zener transitions [42–45], hardly tunable junctions parameters [46–48], lifetime broadening and a finite detection bandwidth [46, 49]. The approach to combine Shapiro measurements with radiation measurements on a single Josephson junction, as in Ref. [50], should greatly reduce ambiguity on its topolog-

* roy.haller@unibas.ch

† <http://www.nanoelectronics.unibas.ch/>

ical nature. Furthermore, the fractional radiation signal can be detected independent of the magnitude of the trivial supercurrent. This contrasts Shapiro step measurements where mainly the ratio of the topological to trivial supercurrent determines its resolvability [24].

In this work, we investigate a gate-tunable Cd_3As_2 nanowire Josephson junction by assessing the dc and the ac Josephson effect. By including thermal fluctuations in the resistively and capacitively shunted junction (RCSJ) model, we successfully reproduce the obtained IV -curves, Josephson emission spectra and Shapiro patterns using only a conventional, sinusoidal 2π -periodic CPR. The comparison enables us to determine the effective electron temperature of the system which, in turn, imposes limitations to the sensitivity and may serve as a possible explanation for the absence of fractional signatures in the ac Josephson effect.

II. DEVICE & MEASUREMENT SETUP

Fig. 1(a) shows the Cd_3As_2 nanowire Josephson junction device connected to the schematic of the measurement setup. The nanowire has a diameter of 50 nm, and the junction has a length of 150 nm that is determined by the spacing of the superconducting Al leads. A locally deposited layer of HfO_2 (20 nm) covering the whole inner part of the chip (see Fig. 1(c)) serves as gate-dielectric for the Au top gate that allows tuning the charge carrier density inside the wire by applying a gate voltage V_{tg} . A cross-sectional cut through the device structure is illustrated in Fig. 1(b).

The measurement setup shown in Fig. 1(a) allows probing the ac Josephson effect in two ways. First, the Josephson radiation emitted from the junction under finite dc bias can be detected directly with a spectrum analyzer. Second, the reverse experiment can be done: irradiating the device with an ac field emitted by a microwave source while measuring the dc transport response of the junction, resulting in Shapiro steps [51]. In this case, a directional coupler feeds the incoming microwave tone to the sample, whereas in the Josephson radiation experiment, it directs the signal emitted by the junction to the spectrum analyzer. The out-coming signal passes through isolator stages, limiting the detection bandwidth to 2.5 – 3.8 GHz, after which the signal gets amplified by a high-electron-mobility-transistor (HEMT).

Our dc setup sources a current using a bias resistor $R_b = 1 \text{ M}\Omega$ in series with a dc voltage source with a small ac component with frequency $f = 177 \text{ Hz}$ supplied by a lock-in amplifier. This current is applied via a bias tee to the microwave line that directly connects to the source of the sample. The other side of the sample is galvanically connected to ground, closing both the low- and high-frequency circuits. When the sample is in the non-superconducting regime, the signal is converted to a stable voltage bias by shunting the device with a resistor $R_s = 10 \Omega$. This shunt resistor is directly placed between

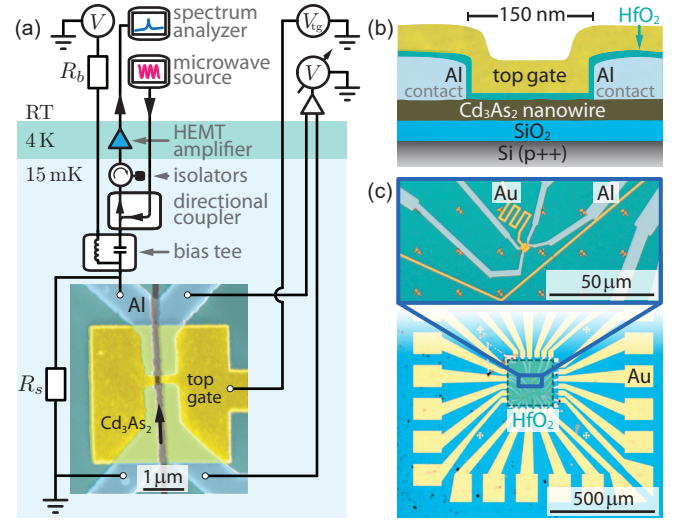


FIG. 1. Device and measurement setup. (a) Cd_3As_2 nanowire Josephson junction embedded in a radiation (irradiation) setup using a spectrum analyzer (microwave source). (Inset) False-colored SEM image of the junction defined by superconducting Al leads (blue) in the Cd_3As_2 nanowire (center axis along black arrow). The top gate electrode (yellow) is isolated from the junction by a 20 nm thick HfO_2 layer. The voltage V_{tg} applied on the Au gate allows tuning the charge carrier density. The junction is shunted by a resistor $R_s = 10 \Omega$ that connects the rf line to the fridge ground on the PCB. (b) Cross-sectional illustration of the junction along the black arrow in (a). (c) Optical image showing the electrodes extending from the junction (top) towards the Au bonding pads shown on the overview of the chip (bottom).

the central conductor of the transmission line and the galvanic ground on the sample holder. We measure the differential resistance of the shunted device using a voltage amplifier and lock-in techniques. All measurements are performed in a dilution refrigerator with a base temperature of $\sim 15 \text{ mK}$.

Details about the fabrication, the measurement setup and the device integration on the PCB are given in the supplementary material (SM) Sec. SII and Sec. SIII [52].

III. MEASUREMENT RESULTS

We first probe the gate dependent dc response of the junction, which is presented in Fig. 2. The differential resistance as a function of current I bias and top gate voltage V_{tg} in Fig. 2(a), reveals a clear switching behavior from a zero resistance superconducting state (black) to a normal resistive state (blue). We attribute the peaks in differential resistance to the critical current I_c , which become sharper and more pronounced for higher I_c as seen in Fig. 2(b). Under sufficiently large current bias the differential resistance approaches R_s . As a function of V_{tg} , we observe an anomalous evolution of I_c ; when sweeping the gate from negative to positive voltages, I_c first in-

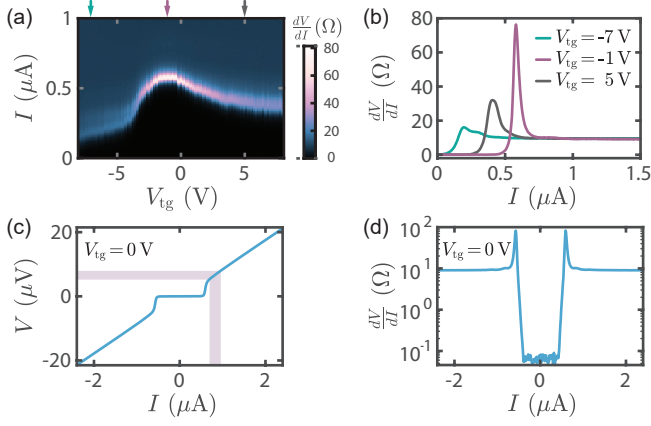


FIG. 2. Gate dependent supercurrent. (a) Differential resistance dV/dI as a function of current bias I and top gate voltage V_{tg} . (b) dV/dI as a function of I at different gate voltages taken from line cut in (a) at the positions indicated by the arrows. The dV/dI -peak position is identified as the critical current I_c . (c) IV -characteristic at $V_{tg} = 0$ V obtained by integrating the measured dV/dI shown in logarithmic scale in (d). The violet shaded area indicates the current and voltage range that produces conventional Josephson radiation in a 2.5 – 3.8 GHz bandwidth.

creases and then decreases again in an asymmetric way with a maximum of $I_c = 580$ nA at $V_{tg} = -1$ V. This behavior contrasts ordinary semiconductor JJs, which generally exhibit a steady increase of the critical current as a function of larger electric-field induced doping. The unusual gate response has been previously reported in long Cd_3As_2 nanowire JJs and has been proposed to originate from scattering mechanisms between surface and bulk states that give rise to dephasing [22]. In this case, one assumes the majority of the supercurrent is carried by surface states and increasing the electron density enhances scattering with bulk modes which, in turn, results in a suppression of the coherent Cooper pair transport, and hence leads to a reduction of I_c . This hypothesis is further supported by the $I_c R_N$ -product discussed in the SM Sec. SV.

In Fig. 2(c), the IV -curve at $V_{tg} = 0$ V, obtained by integrating the measured dV/dI curve presented in Fig. 2(d), shows a clear voltage plateau which we assume is zero. In the normal state, the junction shows ohmic behavior down to $5 \mu\text{V}$, which allows steady voltage biasing in the regime of conventional Josephson radiation for the given detection bandwidth (violet shading).

In the next step, we investigate the Josephson radiation spectrum at $V_{tg} = 0$ V, for which $I_c = 570$ nA. In Fig. 3(a), the normalized power spectral density collected for a 20 MHz bandwidth is plotted as a function of voltage bias V and detection frequency f_{det} . The normalization for each f_{det} allows us to compensate for the frequency dependent background. The detected radiation features are symmetric in voltage and solely determined by conventional Josephson emission arising due to the in-

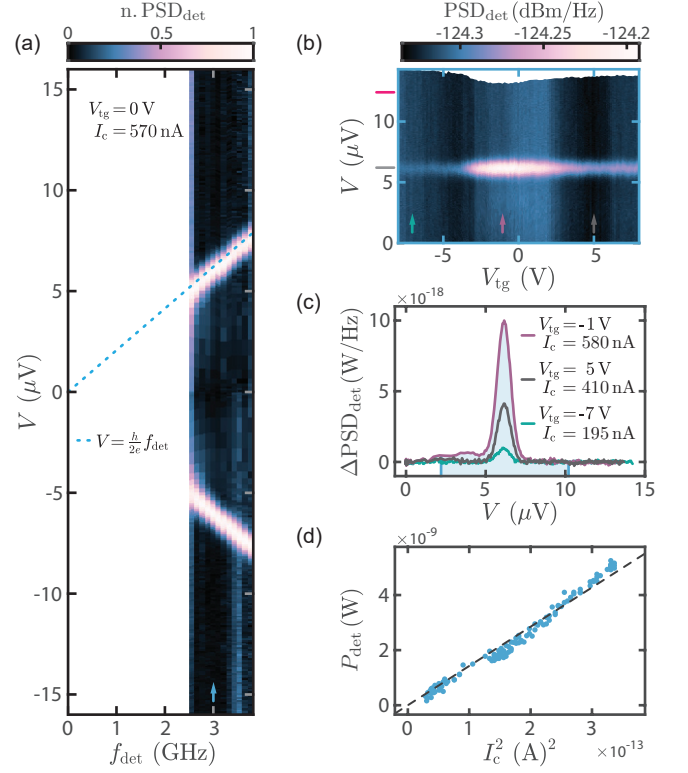


FIG. 3. Emission spectrum. (a) Normalized power spectral density ($n.\text{PSD}_{\text{det}}$) as a function of the voltage drop V across the junction and detection frequencies f_{det} at $V_{tg} = 0$ V. The radiation spectrum is overlaid with the expected peak position of conventional Josephson emission. (b) Power spectral density (PSD_{det}) as a function of V and V_{tg} , measured at a fixed detection frequency $f_{\text{det}} = 3$ GHz indicated by the blue arrow in (a). The gray mark on the voltage axis indicates the expected conventional emission peak position, whereas the pink mark is placed at the position of a potential topologically non-trivial emission peak. (c) PSD_{det} in linear scale with subtracted background ($\Delta\text{PSD}_{\text{det}}$) as a function of V at three gate voltages obtained from line cuts in (b) at the positions indicated by the arrows. (d) Emission strength P_{det} (W) plotted against the corresponding critical current squared (I_c^2).

elastic transfer of Cooper pairs. The signal follows the fundamental ac Josephson relation $V = hf_J/(2e)$, illustrated by the dashed line. When the detection frequency of the spectrum analyzer is aligned with the Josephson frequency ($f_J = f_{\text{det}}$) the power spectral density peaks. Neither signatures from topological supercurrent contributions that would evolve as $V = hf_J/e$, nor clear higher-order emission features are observed. The latter is expected for a Josephson junction possessing a CPR consisting of $\sin(n\varphi)$ -harmonics with $n = 2, 3, 4, \dots$, i.e., a skewed CPR where multiple Cooper pairs counted by n are involved in one effective transfer event [53–57], resulting in higher-order emission peaks following the relation $V = hf_J/(n2e)$. Therefore, we conclude that our junction dynamics are dominated by a sinusoidal 2π -periodic CPR.

Next, we look for the emergence of a topological phase as a function of doping level in Fig. 3(b), where we measured the power spectral density with fixed $f_{\text{det}} = 3 \text{ GHz}$, while sweeping V across the junction for different V_{tg} . We note the voltage position for topologically non-trivial emission ($V = hf_J/e$) in pink, at which no additional radiation peaks appear. The conventional emission peak modulates in intensity but remains visible throughout the whole gate range and aligns to the conventional voltage position ($V = hf_J/2e$) marked in gray.

To estimate a lower bound of sensitivity in terms of I_c , we relate the emission strength to the critical current. We first convert the raw data from dBm/Hz-scale to Watt/Hz-scale and subtract for each gate voltage a linear background such that regions far away from the radiation peaks have vanishing small contributions. The hereby obtained relative emission density ($\Delta\text{PSD}_{\text{det}}$) as a function of V is shown in Fig. 3(c) for different V_{tg} , corresponding to different I_c that are extracted from Fig. 2(a). In Fig. 3(d) we correlate the emission strength P_{det} to the square of the critical current I_c^2 . P_{det} is obtained by integrating $\Delta\text{PSD}_{\text{det}}$ over the voltage interval ($2.2 - 10.2 \mu\text{V}$) that is indicated with the light blue shading in Fig. 3(c) as $P_{\text{det}}(\text{W}) = \frac{2e}{h} \int_{2.2 \mu\text{V}}^{10.2 \mu\text{V}} \Delta\text{PSD}_{\text{det}} [\text{W/Hz}] dV$. We recognize a clear quadratic dependence between P_{det} and I_c . Considering the junction as a sinusoidal ac current source with amplitude I_c , indeed a power $P_{\text{det}} = \mathcal{R}I_c^2/2$ is dissipated in the detector, where \mathcal{R} describes the power transfer ratio, detailed in SM Sec. SIV. From the power to critical current relation, we estimate for the given experimental configuration, a lower detection limit of $I_c \approx 55 \text{ nA}$. This is a potential explanation for the lack of topological signatures in the radiation spectrum since it is known that the associated non-trivial supercurrent in Cd_3As_2 nanowires may only be a small fraction ($\leq 10\%$) of the overall critical current [24].

We now expand the investigation of the ac Josephson effect by measuring the Shapiro step pattern. Here, the junction is irradiated by a microwave tone of fixed frequency $f_d = 2 \text{ GHz}$ at variable output power P_s of the signal generator. We probe the differential resistance dV/dI as a function of current bias I and P_s for a constant gate voltage $V_{\text{tg}} = 0 \text{ V}$. The resulting map shown in Fig. 4(a), reveals the characteristic voltage plateaus in regions of vanishing dV/dI (dark teardrop shapes). With increasing P_s , the 0th-plateau ($V = 0$) diminishes, while higher-order Shapiro steps progressively emerge. In Fig. 4(b) we present the IV -curve obtained by integrating dV/dI for different drive powers, and the voltage axis in units of the Shapiro voltage matches with the measured voltage steps. By numerically differentiating the interpolated IV -curves we can extract the differential conductance dI/dV , which is presented in Fig. 4(c) as a function of V and P_s for different top gate voltages. With this visualization technique, no binning is required and the resolution is maintained [58]. The voltage plateaus appear as lines in the color map, whereas their intensities reflect the width of the Shapiro steps. In agreement with the

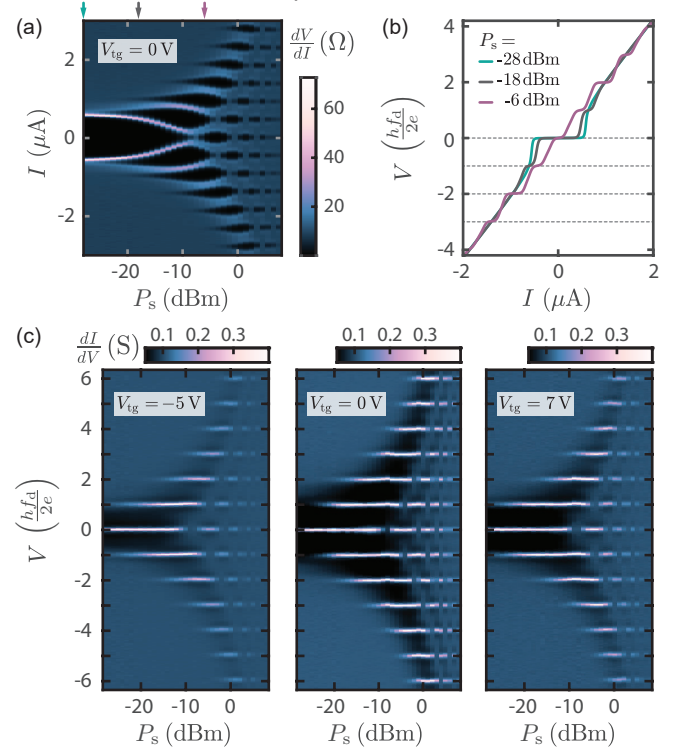


FIG. 4. Shapiro step measurement with drive frequency $f_d = 2 \text{ GHz}$. (a) Differential resistance dV/dI as a function of drive power P_s at the microwave source and current bias I . (b) IV -curves obtained by integrating dV/dI for irradiation powers indicated by the arrows in (a), with the voltage axis normalized to the Shapiro step voltage $hf_d/2e$. (c) Differential conductance dI/dV as a function of P_s and V in units of the Shapiro step voltage $hf_d/2e$, measured on the hole side ($V_{\text{tg}} = -5 \text{ V}$), the electron side ($V_{\text{tg}} = 7 \text{ V}$), and close to the Dirac point ($V_{\text{tg}} = 0 \text{ V}$). Data is numerically converted from current-biased data; the center map constitutes the same measurement as (a).

lack of topological signatures in the radiation measurement, no modulation in the width of subsequent steps is observed in the experimentally accessed parameter space, as evaluated in the SM Sec. SVI.

IV. RCSJ SIMULATION WITH THERMAL FLUCTUATIONS

To gain a deeper understanding of the junction dynamics, we aim to reproduce our experimental results in the framework of the resistively and capacitively shunted junction (RCSJ) model. To be able to reproduce our experimental data, we include a noise term to account for thermal fluctuations [59]. Consequently, the model [60], which is detailed in the SM Sec. SI contains the following parameters: the critical current I_c , the shunt resistance R , the shunt capacitance C and the effective temperature T . Furthermore, the shape of the CPR matters, which in the following is set to a sinusoidal, 2π -periodic function

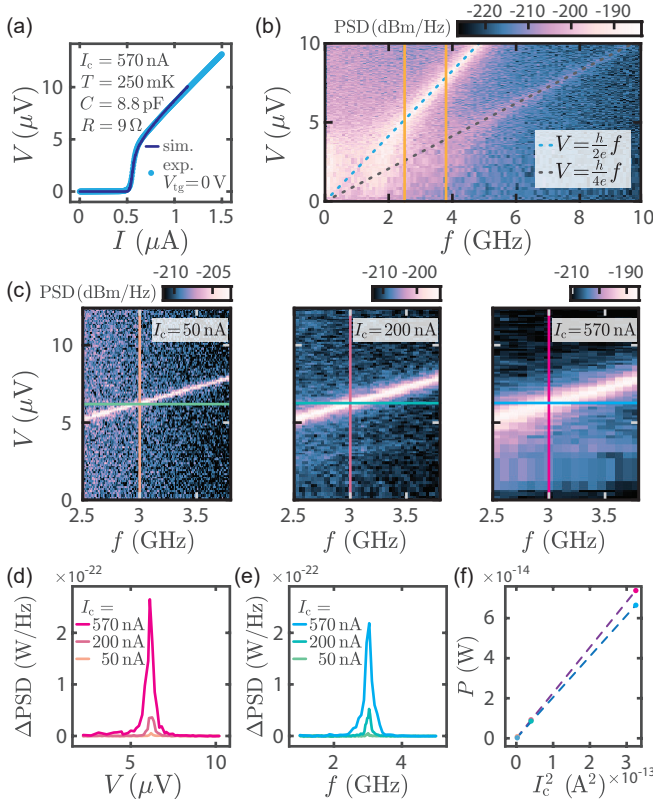


FIG. 5. Results of RCSJ modeling with thermal fluctuations. (a) Simulated IV -characteristics (dark blue) fitted to the experimental curve at $V_{tg} = 0$ V (light blue). The fit parameters: critical current I_c , effective temperature T , shunt capacitance C , and shunt resistance R are listed. T, C, R are kept constant for the subsequent plots. (b) Simulated power spectral density (PSD) as a function of mean voltage V and frequency f deduced from the voltage evolution in time for $I_c = 570$ nA. The map is overlaid with the fundamental (blue) voltage-to-frequency conversion and the first higher-harmonic (gray). The orange vertical lines indicate the frequency range (2.5–3.8 GHz) of interest for the comparison with the experiment. (c) Simulated emission spectrum for different I_c . (d-e) PSD in linear scale with subtracted background (ΔPSD) for different I_c deduced from the maps presented in (c) for a given frequency and voltage, respectively. In (d) $f=3$ GHz and in (e) its voltage equivalent $V = 6.2 \mu\text{V}$ that relate to vertical and horizontal cuts presented in (c). (f) Emission strength P plotted against the corresponding critical current squared (I_c^2) by integrating over the voltage (P_V , red) and by integrating over the frequency (P_f , blue).

$I_s = I_c \sin(\varphi)$, where φ represents the phase drop and I_s the supercurrent across the junction. The discussion is extended to admixtures of 2π - and 4π -periodic CPRs in the SM Sec. SI.

The output of the model is the time evolution of the junction phase $\varphi(t)$, from which the junction voltage is calculated using the ac Josephson relation, $V(t) = \frac{\hbar}{2e} \frac{d\varphi(t)}{dt}$ with $\hbar = h/2\pi$. First, we consider the time-averaged results of the modified RCSJ model to fit the experimentally obtained IV -curve at $V_{tg} = 0$ V

as presented in Fig. 5(a). With the hereby obtained model parameters that are listed in the plot, a junction quality factor $Q = \sqrt{2eI_c/(\hbar C)} \cdot RC \approx 1$ is obtained, which classifies the junction into the intermediately damped regime [61], which is further supported by the smooth switching behavior accompanied with a negligible hysteresis between up/down current bias sweeps (not shown). The elevated effective temperature ($T = 250$ mK) with respect to the base temperature ($T_b = 15$ mK) originates from external noise, likely generated by the HEMT configured at a sub-optimal operating point, an issue that was only later identified.

In the next step, we employ the extracted parameters and focus on the time-dependent $V(t)$ solutions of the RCSJ model to reproduce the emission spectrum. By taking the squared magnitude of the Fourier transform of $V(t)$, we calculate the voltage noise spectral density as a function of frequency f , and convert it to power spectral density (PSD). Here, we do not include any amplification of the signal; the comparison of absolute signal levels between the experiment and simulation is discussed in the SM Sec. SIV. In Fig. 5(b) we plot the simulated PSD as a function of f and averaged voltage V . Within the experimentally accessible range, indicated by the orange lines, the simulation qualitatively reproduces the detected emission spectrum previously presented in Fig. 3(a). Interestingly, the simulation reveals, in addition to the conventional voltage to frequency relation (blue dashed), an emission peak at double the frequency for a given voltage (gray dashed). We attribute this feature to the current bias in our model, leading to higher order modes of frequency $f = n2eV/h$ [56]. In this manner, higher-order features can be generated from a purely sinusoidal CPR, as seen in the simulations for different model parameters presented in the SM Sec. SI.

We now direct our attention to the modeled emission strength as a function of I_c . Fig. 5(c) shows simulated radiation maps for increasing I_c , with f corresponding to our experimental range. For each I_c we generate voltage linecuts for fixed $f = 3$ GHz (orange, pink, magenta lines), and extract their corresponding frequency linecuts for fixed $V = 6.2 \mu\text{V}$ (green, aqua, blue). In Fig. 5(d) and (e) we evaluate ΔPSD by subtracting a linear background for the voltage-cuts and a $1/f$ background for the frequency-cuts, from which we obtain the emission strength of the junction: (i) By integrating ΔPSD over the voltage interval (2.2–10.2 μV) as $P_V(\text{W}) = \frac{2e}{h} \int_{2.2 \mu\text{V}}^{10.2 \mu\text{V}} \Delta\text{PSD} [\text{W/Hz}] dV$ and (ii) by integrating ΔPSD over the voltage corresponding frequency interval (1–5 GHz) as $P_f(\text{W}) = \int_{1 \text{ GHz}}^{5 \text{ GHz}} \Delta\text{PSD} [\text{W/Hz}] df$. The hereby obtained emission strength is linearly correlated to I_c^2 as illustrated in Fig. 5(f), where the procedure via integration over the voltage (frequency) is shown in red (blue) color. We attributed the slightly enhanced emission strength obtained from the voltage integration procedure to higher-order contributions appearing at integer fractions of the main emission peak.

By adding an ac current bias excitation in the RCSJ

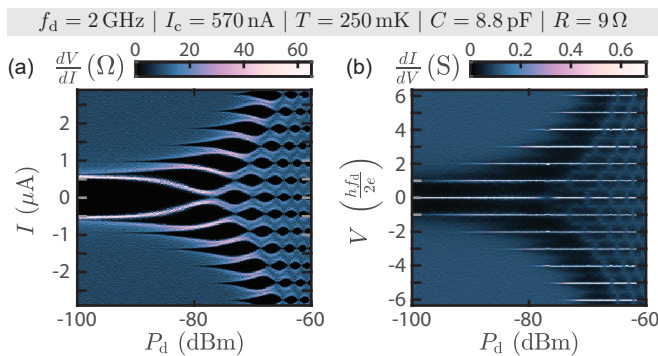


FIG. 6. Simulated Shapiro pattern reproducing the experimentally obtained features at $V_{\text{ig}} = 0 \text{ V}$ presented in Fig. 4. The parameters used in the RCSJ model with thermal fluctuations are listed. (a) Differential resistance dV/dI as a function of drive power P_d at the device and current bias I . (b) Differential conductance dI/dV as a function of P_d and V in units of the Shapiro step voltage $h f_d / 2e$.

model expressed in drive power P_d at the device, it is also capable of generating Shapiro step patterns. Employing the same model parameters as before, we find good agreement in the Shapiro pattern between the simulation presented in Fig. 6 and the experiment shown in Fig. 4, again by using a 2π -periodic sinusoidal CPR. In the SM Sec. SVI we analyze simulated Shapiro step patterns with CPRs containing an admixture of topologically non-trivial $\sin(\varphi/2)$ CPR contributions. In contrast to the evaluation of the radiation experiment, where an absolute detection limit can be defined, with the step width analysis a relative detection threshold can be established. For the specific parameters used, we find that below a topological to conventional CPR ratio of $\sim 10\%$, the topological features are masked by the dominating 2π -periodic supercurrent.

V. CONCLUSION

We investigated the dc and ac Josephson effect in a single Cd_3As_2 nanowire Josephson junction. Although we observe an anomalous evolution of the critical current as a function of gate voltage that points to the presence of supercurrent carrying surface states, no direct evidence of topological superconductivity is found in both the Josephson radiation measurement and Shapiro

pattern evaluation. Importantly, we reproduce our experimental findings using a refined RCSJ model that includes thermal fluctuations, and we obtain an effective electronic temperature $T \approx 250 \text{ mK}$ which masks emission signals from supercurrents $< 55 \text{ nA}$, highlighting the importance of reducing thermal noise.

The work on $(\text{Bi}_{1-x}\text{Sb}_x)_2\text{Te}_3$ [50] similarly finds no evidence of the fractional Josephson effect, which they attribute to a large shunt capacitance that reduces the power reaching their detector. We face similar detection limit challenges which could be overcome by improving the filtering, minimizing the ground noise, matching the junction and detector impedance, optimizing the detector settings, and adding a Josephson parametric amplifier to the amplification chain. The resulting gain in the signal-to-noise ratio hopefully allows us to resolve much lower supercurrents and reveal the topological nature of these materials.

ACKNOWLEDGMENTS

We are grateful for scientific discussions with Chuan Li. This research was supported by the Swiss National Science Foundation through a) grants No 172638 and 192027, b) the National Centre of Competence in Research Quantum Science and Technology (QSIT), and c) the QuantEra project SuperTop; the János Bolyai Research Scholarship of the Hungarian Academy of Sciences, the National Research Development and Innovation Office (NKFIH) through the OTKA Grants FK 132146 and NN127903 (FlagERA Topograph), and the National Research, Development and Innovation Fund of Hungary within the Quantum Technology National Excellence Program (Project Nr. 2017-1.2.1-NKP-2017-00001), the Quantum Information National Laboratory of Hungary and the ÚNKP-22-5 New National Excellence Program. We further acknowledge funding from the European Union's Horizon 2020 research and innovation program, specifically a) from the European Research Council (ERC) grant agreement No 787414, ERC-Adv TopSupra, b) grant agreement No. 862046, FET TOP-SQUAD and c) grant agreement No 828948, FET-open project AndQC. M.J. is supported by the midcareer research program (NRF-2023R1A2C1004832) through the National Research Foundation of Korea (NRF) grant.

All raw- and metadata in this publication are available in numerical form together with the processing codes at DOI: 10.5281/zenodo.7961884.

- [1] A. Y. Kitaev, Unpaired Majorana fermions in quantum wires, *Physics-Uspekhi* **44**, 131 (2001).
- [2] A. Kitaev, Fault-tolerant quantum computation by anyons, *Annals of Physics* **303**, 2 (2003).
- [3] D. A. Ivanov, Non-Abelian Statistics of Half-Quantum Vortices in p -Wave Superconductors, *Phys. Rev. Lett.* **86**, 268 (2001).

- [4] C. Nayak, S. H. Simon, A. Stern, M. Freedman, and S. Das Sarma, Non-Abelian anyons and topological quantum computation, *Rev. Mod. Phys.* **80**, 1083 (2008).
- [5] F. Wilczek, Majorana returns, *Nat. Phys.* **5**, 614 (2009).
- [6] A. Stern and N. H. Lindner, Topological Quantum Computation – From Basic Concepts to First Experiments, *Science* **339**, 1179 (2013).

- [7] T. Karzig, C. Knapp, R. M. Lutchyn, P. Bonderson, M. B. Hastings, C. Nayak, J. Alicea, K. Flensberg, S. Plugge, Y. Oreg, C. M. Marcus, and M. H. Freedman, Scalable designs for quasiparticle-poisoning-protected topological quantum computation with Majorana zero modes, *Phys. Rev. B* **95**, 235305 (2017).
- [8] L. Fu and C. L. Kane, Josephson current and noise at a superconductor/quantum-spin-Hall-insulator/superconductor junction, *Phys. Rev. B* **79**, 161408(R) (2009).
- [9] R. M. Lutchyn, J. D. Sau, and S. Das Sarma, Majorana Fermions and a Topological Phase Transition in Semiconductor-Superconductor Heterostructures, *Phys. Rev. Lett.* **105**, 077001 (2010).
- [10] J. D. Sau, R. M. Lutchyn, S. Tewari, and S. Das Sarma, Generic New Platform for Topological Quantum Computation Using Semiconductor Heterostructures, *Phys. Rev. Lett.* **104**, 040502 (2010).
- [11] J. Alicea, Majorana fermions in a tunable semiconductor device, *Phys. Rev. B* **81**, 125318 (2010).
- [12] X. L. Qi and S. C. Zhang, Topological insulators and superconductors, *Rev. Mod. Phys.* **83**, 1057 (2011).
- [13] S. M. Frolov, M. J. Manfra, and J. D. Sau, Topological superconductivity in hybrid devices, *Nature Physics* **16**, 718 (2020).
- [14] S. M. Young, S. Zaheer, J. C. Y. Teo, C. L. Kane, E. J. Mele, and A. M. Rappe, Dirac Semimetal in Three Dimensions, *Phys. Rev. Lett.* **108**, 140405 (2012).
- [15] Z. Wang, Y. Sun, X.-Q. Chen, C. Franchini, G. Xu, H. Weng, X. Dai, and Z. Fang, Dirac semimetal and topological phase transitions in $A_3\text{Bi}$ ($A = \text{Na}, \text{K}, \text{Rb}$), *Phys. Rev. B* **85**, 195320 (2012).
- [16] Z. Wang, H. Weng, Q. Wu, X. Dai, and Z. Fang, Three-dimensional Dirac semimetal and quantum transport in Cd_3As_2 , *Phys. Rev. B* **88**, 125427 (2013).
- [17] A. Burkov, Topological semimetals, *Nature materials* **15**, 1145 (2016).
- [18] N. P. Armitage, E. J. Mele, and A. Vishwanath, Weyl and Dirac semimetals in three-dimensional solids, *Rev. Mod. Phys.* **90**, 015001 (2018).
- [19] I. Crassee, R. Sankar, W.-L. Lee, A. Akrap, and M. Orlita, 3D Dirac semimetal Cd_3As_2 : A review of material properties, *Phys. Rev. Mater.* **2**, 120302 (2018).
- [20] S. Jeon, B. B. Zhou, A. Gyenis, B. E. Feldman, I. Kimchi, A. C. Potter, Q. D. Gibson, R. J. Cava, A. Vishwanath, and A. Yazdani, Landau quantization and quasiparticle interference in the three-dimensional Dirac semimetal Cd_3As_2 , *Nat. Mater.* **13**, 851 (2014).
- [21] A. Chen, D. I. Pikulin, and M. Franz, Josephson current signatures of Majorana flat bands on the surface of time-reversal-invariant Weyl and Dirac semimetals, *Phys. Rev. B* **95**, 174505 (2017).
- [22] C. Z. Li, C. Li, L. X. Wang, S. Wang, Z. M. Liao, A. Brinkman, and D. P. Yu, Bulk and surface states carried supercurrent in ballistic Nb-Dirac semimetal Cd_3As_2 nanowire-Nb junctions, *Phys. Rev. B* **97**, 115446 (2018).
- [23] W. Yu, W. Pan, D. L. Medlin, M. A. Rodriguez, S. R. Lee, Z.-q. Bao, and F. Zhang, π and 4π Josephson Effects Mediated by a Dirac Semimetal, *Phys. Rev. Lett.* **120**, 177704 (2018).
- [24] A.-Q. Wang, C.-Z. Li, C. Li, Z.-M. Liao, A. Brinkman, and D.-P. Yu, 4π -Periodic Supercurrent from Surface States in Cd_3As_2 Nanowire-Based Josephson Junctions, *Phys. Rev. Lett.* **121**, 237701 (2018).
- [25] H.-J. Kwon, K. Sengupta, and V. M. Yakovenko, Fractional ac Josephson effect in p - and d -wave superconductors, *Eur. Phys. J. B* **37**, 349 (2004).
- [26] J.-J. Feng, Z. Huang, Z. Wang, and Q. Niu, Josephson radiation from nonlinear dynamics of Majorana zero modes, *Phys. Rev. B* **101**, 180504(R) (2020).
- [27] F. Domínguez, F. Hassler, and G. Platero, Dynamical detection of Majorana fermions in current-biased nanowires, *Phys. Rev. B* **86**, 140503(R) (2012).
- [28] F. Domínguez, O. Kashuba, E. Bocquillon, J. Wiedenmann, R. S. Deacon, T. M. Klapwijk, G. Platero, L. W. Molenkamp, B. Trauzettel, and E. M. Hankiewicz, Josephson junction dynamics in the presence of 2π - and 4π -periodic supercurrents, *Phys. Rev. B* **95**, 195430 (2017).
- [29] J. Picó-Cortés, F. Domínguez, and G. Platero, Signatures of a 4π -periodic supercurrent in the voltage response of capacitively shunted topological Josephson junctions, *Phys. Rev. B* **96**, 125438 (2017).
- [30] L. P. Rokhinson, X. Liu, and J. K. Furdyna, The fractional ac Josephson effect in a semiconductor-superconductor nanowire as a signature of Majorana particles, *Nature Physics* **8**, 795 (2012).
- [31] K. Le Calvez, L. Veyrat, F. Gay, P. Plaindoux, C. B. Winkelmann, H. Courtois, and B. Sacépé, Joule overheating poisons the fractional ac Josephson effect in topological Josephson junctions, *Communications Physics* **2**, 4 (2019).
- [32] P. Schüffegen, D. Rosenbach, C. Li, T. W. Schmitt, M. Schleenvoigt, A. R. Jalil, S. Schmitt, J. Kölzer, M. Wang, B. Bennemann, *et al.*, Selective area growth and stencil lithography for in situ fabricated quantum devices, *Nature nanotechnology* **14**, 825 (2019).
- [33] R. Yano, M. Koyanagi, H. Kashiwaya, K. Tsumura, H. T. Hirose, Y. Asano, T. Sasagawa, and S. Kashiwaya, Unusual Superconducting Proximity Effect in Magnetically Doped Topological Josephson Junctions, *J. Phys. Soc. Jpn.* **89**, 034702 (2020).
- [34] J. Wiedenmann, E. Bocquillon, R. S. Deacon, S. Hartinger, O. Herrmann, T. M. Klapwijk, L. Maier, C. Ames, C. Brüne, C. Gould, A. Oiwa, K. Ishibashi, S. Tarucha, H. Buhmann, and L. W. Molenkamp, 4π -periodic Josephson supercurrent in HgTe-based topological Josephson junctions, *Nat. Commun.* **7**, 10303 (2016).
- [35] E. Bocquillon, R. S. Deacon, J. Wiedenmann, P. Leubner, T. M. Klapwijk, C. Brüne, K. Ishibashi, H. Buhmann, and L. W. Molenkamp, Gapless Andreev bound states in the quantum spin Hall insulator HgTe, *Nature Nanotechnology* **12**, 137 (2017).
- [36] C. Li, J. C. de Boer, B. de Ronde, S. V. Ramankutty, E. van Heumen, Y. Huang, A. de Visser, A. A. Golubov, M. S. Golden, and A. Brinkman, 4π -periodic Andreev bound states in a Dirac semimetal, *Nature materials* **17**, 875 (2018).
- [37] M. Bai, X.-K. Wei, J. Feng, M. Luysberg, A. Bliesener, G. Lippertz, A. Uday, A. A. Taskin, J. Mayer, and Y. Ando, Proximity-induced superconductivity in $(\text{Bi}_{1-x}\text{Sb}_x)_2\text{Te}_3$ topological-insulator nanowires, *Communications Materials* **3**, 20 (2022).
- [38] R. S. Deacon, J. Wiedenmann, E. Bocquillon, F. Domínguez, T. M. Klapwijk, P. Leubner, C. Brüne, E. M. Hankiewicz, S. Tarucha, K. Ishibashi, H. Buhmann, and L. W. Molenkamp, Josephson Radiation from Gapless Andreev Bound States in HgTe-Based Topological Junctions, *Phys. Rev. X* **7**, 021011 (2017).

- [39] D. Laroche, D. Bouman, D. J. van Woerkom, A. Proutski, C. Murthy, D. I. Pikulin, C. Nayak, R. J. J. van Gulik, J. Nygård, P. Krogstrup, L. P. Kouwenhoven, and A. Geresdi, Observation of the 4π -periodic Josephson effect in indium arsenide nanowires, *Nat. Commun.* **10**, 245 (2019).
- [40] H. Kamata, R. S. Deacon, S. Matsuo, K. Li, S. Jeppesen, L. Samuelson, H. Q. Xu, K. Ishibashi, and S. Tarucha, Anomalous modulation of Josephson radiation in nanowire-based Josephson junctions, *Phys. Rev. B* **98**, 041302(R) (2018).
- [41] S. R. Mudi and S. M. Frolov, Model for missing Shapiro steps due to bias-dependent resistance (2022), arXiv:2106.00495 [cond-mat.mes-hall].
- [42] P.-M. Billangeon, F. Pierre, H. Bouchiat, and R. Deblock, ac Josephson Effect and Resonant Cooper Pair Tunneling Emission of a Single Cooper Pair Transistor, *Phys. Rev. Lett.* **98**, 216802 (2007).
- [43] M. C. Dartailh, J. J. Cuoizzo, B. H. Elfeky, W. Mayer, J. Yuan, K. S. Wickramasinghe, E. Rossi, and J. Shabani, Missing Shapiro steps in topologically trivial Josephson junction on InAs quantum well, *Nature Communications* **12**, 78 (2021).
- [44] I. T. Rosen, C. J. Trimble, M. P. Andersen, E. Mikheev, Y. Li, Y. Liu, L. Tai, P. Zhang, K. L. Wang, Y. Cui, M. A. Kastner, J. R. Williams, and D. Goldhaber-Gordon, Fractional AC Josephson effect in a topological insulator proximitized by a self-formed superconductor (2021), arXiv:2110.01039 [cond-mat.mes-hall].
- [45] B. H. Elfeky, J. J. Cuoizzo, N. Lotfizadeh, W. F. Schiela, S. M. Farzaneh, W. M. Strickland, D. Langone, E. Rossi, and J. Shabani, Evolution of 4π -Periodic Supercurrent in the Presence of an In-Plane Magnetic Field, *ACS Nano* **17**, 4650 (2023).
- [46] M. Houzet, J. S. Meyer, D. M. Badiane, and L. I. Glazman, Dynamics of Majorana States in a Topological Josephson Junction, *Phys. Rev. Lett.* **111**, 046401 (2013).
- [47] J. Park, Y.-B. Choi, G.-H. Lee, and H.-J. Lee, Characterization of Shapiro steps in the presence of a 4π -periodic Josephson current, *Phys. Rev. B* **103**, 235428 (2021).
- [48] Y. Jang and Y.-J. Doh, Optimal conditions for observing fractional Josephson effect in topological Josephson junctions, *J. Korean Phys. Soc.* **78**, 58 (2021).
- [49] P. San-Jose, E. Prada, and R. Aguado, ac Josephson Effect in Finite-Length Nanowire Junctions with Majorana Modes, *Phys. Rev. Lett.* **108**, 257001 (2012).
- [50] Y. Takeshige, S. Matsuo, R. S. Deacon, K. Ueda, Y. Sato, Y. F. Zhao, L. Zhou, C. Z. Chang, K. Ishibashi, and S. Tarucha, Experimental study of ac Josephson effect in gate-tunable $(\text{Bi}_{1-x}\text{Sb}_x)_2\text{Te}_3$ thin-film Josephson junctions, *Phys. Rev. B* **101**, 115410 (2020).
- [51] S. Shapiro, Josephson Currents in Superconducting Tunneling: The Effect of Microwaves and Other Observations, *Phys. Rev. Lett.* **11**, 80 (1963).
- [52] See Supplemental Material for details about the RCSJ model (SI), the device fabrication (SII), the measurement setup (SIH); valuations of the Josephson emission power (SIV), the $I_c R_N$ product (SV); the evaluation of Shapiro patterns (SVI).
- [53] T. T. Heikkilä, J. Särkkä, and F. K. Wilhelm, Supercurrent-carrying density of states in diffusive mesoscopic Josephson weak links, *Phys. Rev. B* **66**, 184513 (2002).
- [54] M. Chauvin, P. vom Stein, H. Pothier, P. Joyez, M. E. Huber, D. Esteve, and C. Urbina, Superconducting Atomic Contacts under Microwave Irradiation, *Phys. Rev. Lett.* **97**, 067006 (2006).
- [55] A. H. Dayem and C. C. Grimes, Microwave emission from superconducting point-contacts, *Appl. Phys. Lett.* **9**, 47 (1966).
- [56] L. Bretheau, *Localized excitations in superconducting atomic contacts: Probing the Andreev doublet*, Theses, Ecole Polytechnique X (2013).
- [57] J. Basset, M. Kuzmanović, P. Virtanen, T. T. Heikkilä, J. Estève, J. Gabelli, C. Strunk, and M. Aprili, Nonadiabatic dynamics in strongly driven diffusive Josephson junctions, *Phys. Rev. Res.* **1**, 032009(R) (2019).
- [58] J. Ridderbos, M. Brauns, A. Li, E. P. A. M. Bakkers, A. Brinkman, W. G. van der Wiel, and F. A. Zwanenburg, Multiple Andreev reflections and Shapiro steps in a Ge-Si nanowire Josephson junction, *Phys. Rev. Mater.* **3**, 084803 (2019).
- [59] R. L. Kautz and J. M. Martinis, Noise-affected I - V curves in small hysteretic Josephson junctions, *Phys. Rev. B* **42**, 9903 (1990).
- [60] Python code of the RCSJ model is available on https://github.com/donfuge/rcsj_sde.
- [61] W. C. Stewart, Current-voltage characteristics of Josephson junctions, *Appl. Phys. Lett.* **12**, 277 (1968).

Supplementary Material: AC Josephson effect in a gate-tunable Cd₃As₂ nanowire superconducting weak link

SI. MODELING

In the RCSJ model [S1] the junction phase φ is governed by the following differential equation [S2, S3]:

$$\frac{\hbar}{2e} C \frac{d^2 \varphi}{dt^2} + \frac{\hbar}{2e} \frac{1}{R} \frac{d\varphi}{dt} + I_c f(\varphi) + I_F(t) = I(t), \quad (\text{S1})$$

where C is the junction capacitance, R is the parallel resistance, $f(\varphi)$ is the dimensionless shape of the current-phase relation, I_c is the critical current, $I_F(t)$ is the fluctuating noise term, and $I(t) = I_{dc} + I_{ac} \sin(\omega t)$ is the bias current.

To be able to accommodate a mixture of a trivial and a topological supercurrent contribution in the current-phase relation, we set

$$f(\varphi) = a \sin(\varphi) + b \sin(\varphi/2), \quad (\text{S2})$$

where we encode the weight of the two components in the dimensionless parameters a and b . We remark that if both a and b are non-zero, the maximal supercurrent can be larger than the I_c parameter. We assume thermal noise for $I_F(t)$, which is characterized by

$$\langle I_F(t) \rangle = 0 \quad (\text{S3})$$

$$\langle I_F(t) I_F(t') \rangle = \frac{2k_B T}{R} \delta(t - t'), \quad (\text{S4})$$

where $\delta(x)$ is the Dirac function. Let us introduce the normalized units $i = I/I_c$, $i_F = I_F/I_c$ and $\tau = t/t_c$, with

$$t_c = \left(\frac{2e}{\hbar} I_c R \right)^{-1}. \quad (\text{S5})$$

Using these normalized units, the differential equation takes the form of

$$\frac{1}{\beta} \frac{d^2 \varphi}{d\tau^2} + \frac{d\varphi}{d\tau} + f(\varphi) - i(\tau) + i_F(\tau) = 0, \quad (\text{S6})$$

where β is the Stewart-McCumber parameter,

$$\beta = \frac{2e}{\hbar} I_c R^2 C. \quad (\text{S7})$$

The noise term in normalized units satisfies

$$\langle i_F(\tau) \rangle = 0 \quad (\text{S8})$$

$$\langle i_F(\tau) i_F(\tau') \rangle = \frac{2e}{\hbar} \frac{2k_B T}{I_c} \delta(\tau - \tau') = \sigma^2 \delta(\tau - \tau'). \quad (\text{S9})$$

The second-order differential equation in S6 can be written as two coupled first-order equations. By introducing $\mathbf{y} = [\varphi, \dot{\varphi}]^T$, where $\dot{\varphi} = d\varphi/d\tau$, we write S6 as

$$\dot{y}_0 = y_1 \quad (\text{S10})$$

$$\dot{y}_1 = \frac{1}{\beta} (i(\tau) - f(y_0) - y_1 + i_F(\tau)) \quad (\text{S11})$$

Let us write the equation set in a matrix form, and separate the deterministic and random terms,

$$d\mathbf{y} = \mathbf{F}(\mathbf{y}, \tau) d\tau + \mathbf{G}(\mathbf{y}, \tau) d\mathbf{W}, \quad (\text{S12})$$

where $d\mathbf{W}$ is the random noise originating from the current fluctuations, and

$$\mathbf{F}(\mathbf{y}, \tau) = \begin{pmatrix} (i(\tau) - f(y_0) - y_1) / \beta \end{pmatrix} \quad (\text{S13})$$

$$\mathbf{G}(\mathbf{y}, \tau) \equiv \mathbf{G} = \begin{pmatrix} 0 \\ \sigma / \beta \end{pmatrix}. \quad (\text{S14})$$

For the simulations, we calculate the time evolution of $\mathbf{y}(\tau)$ numerically, using Heun's method [S4]. We set the initial conditions, $\mathbf{y}[0] = \mathbf{y}_0$, and calculate $\mathbf{y}[n+1]$ from $\mathbf{y}[n]$ using the following update rules:

$$\mathbf{f}_1 = \mathbf{F}(\mathbf{y}[n]) \cdot h \quad (\text{S15})$$

$$\mathbf{k} = \mathbf{y}[n] + \mathbf{f}_1 \quad (\text{S16})$$

$$\mathbf{f}_2 = \mathbf{F}(\mathbf{k}) \cdot h \quad (\text{S17})$$

$$\mathbf{y}[n+1] = \mathbf{y}[n] + (\mathbf{f}_1 + \mathbf{f}_2)/2 + \mathbf{G}\delta W, \quad (\text{S18})$$

where h is the size of the time step, and δW is a random number sampled from a Gaussian distribution with zero mean and variance h , independently for each time step. For the IV -curve, we calculate the DC voltage on the junction with Josephson's equation using the time-averaged $\varphi(t)$,

$$V = \frac{\hbar}{2e} \left\langle \frac{d\varphi(t)}{dt} \right\rangle = \frac{\hbar}{2e} \frac{1}{t_c} \langle y_1(\tau) \rangle. \quad (\text{S19})$$

We use the `scipy.signal.welch` implementation of the Welch method [S5] in the scipy Python package to calculate the power spectral density (PSD) of the junction voltage $V(t) = (\hbar/2e) \cdot d\varphi(t)/dt$. Then, we convert the PSD from V^2/Hz to dBm/Hz using the formula

$$\text{PSD} [\text{dBm}/\text{Hz}] = 10 \cdot \log_{10} \left(\frac{\text{PSD} [\text{V}^2/\text{Hz}]}{50 \Omega} \right) + 30. \quad (\text{S20})$$

Having the model established we now explore parts of the parameter space, namely, we consider different compositions of the current-phase relation determined by the normalized amplitudes a and b describing a conventional $a \sin(\varphi)$ component added to a topologically non-trivial $b \sin(\varphi/2)$ component. In Fig. S1 and Fig. S2 we display the radiation spectra resulting from the simulation for fixed I_c and R . The blank or blurry regions at low voltages are due to a sudden jump or transition in the IV -characteristics for the specific parameter. In Fig. S1 we investigate the Josephson emission as a function of effective electronic temperature T at fixed C , and in Fig. S2 we investigate the dependence on the shunt capacitance C at fixed T . In the purely conventional case ($a = 1$ and $b = 0$), the lines of strong radiation follow the Josephson relation $V = hf/(n \cdot 2e)$, where $n = 1, 2, 3, \dots$, whereas in the purely topological case ($a = 0$ and $b = 1$), we clearly observe fractions in the radiation pattern following the relation $V = hf/(n \cdot e)$. In both cases, the $n = 1$ line is the most dominant, and higher-order lines weaken with increasing n . In the mixed case ($a \neq 0$ and $b \neq 0$), both sets of lines appear, with weights defined by the parameters a and b .

In the temperature dependence (Fig. S1), we note an increasing noise floor for increasing temperatures. Eventually, small radiative features are hidden in the noise floor, which explains the transition from a rich emission spectrum at low temperature to a spectrum in which only the single, most dominant line is discernible at elevated temperature.

In the capacitance dependence (Fig. S2), we observe a suppression of high-order signatures for a larger shunt capacitance. In addition, we note a reduction of the noise floor and the overall signal. Hence, although the radiation spectrum becomes cleaner for larger C , the emitted signal eventually becomes too small to be detected in a standard amplification chain, which could be a motivation to employ quantum-limited parametric amplifiers in a Josephson radiation setup.

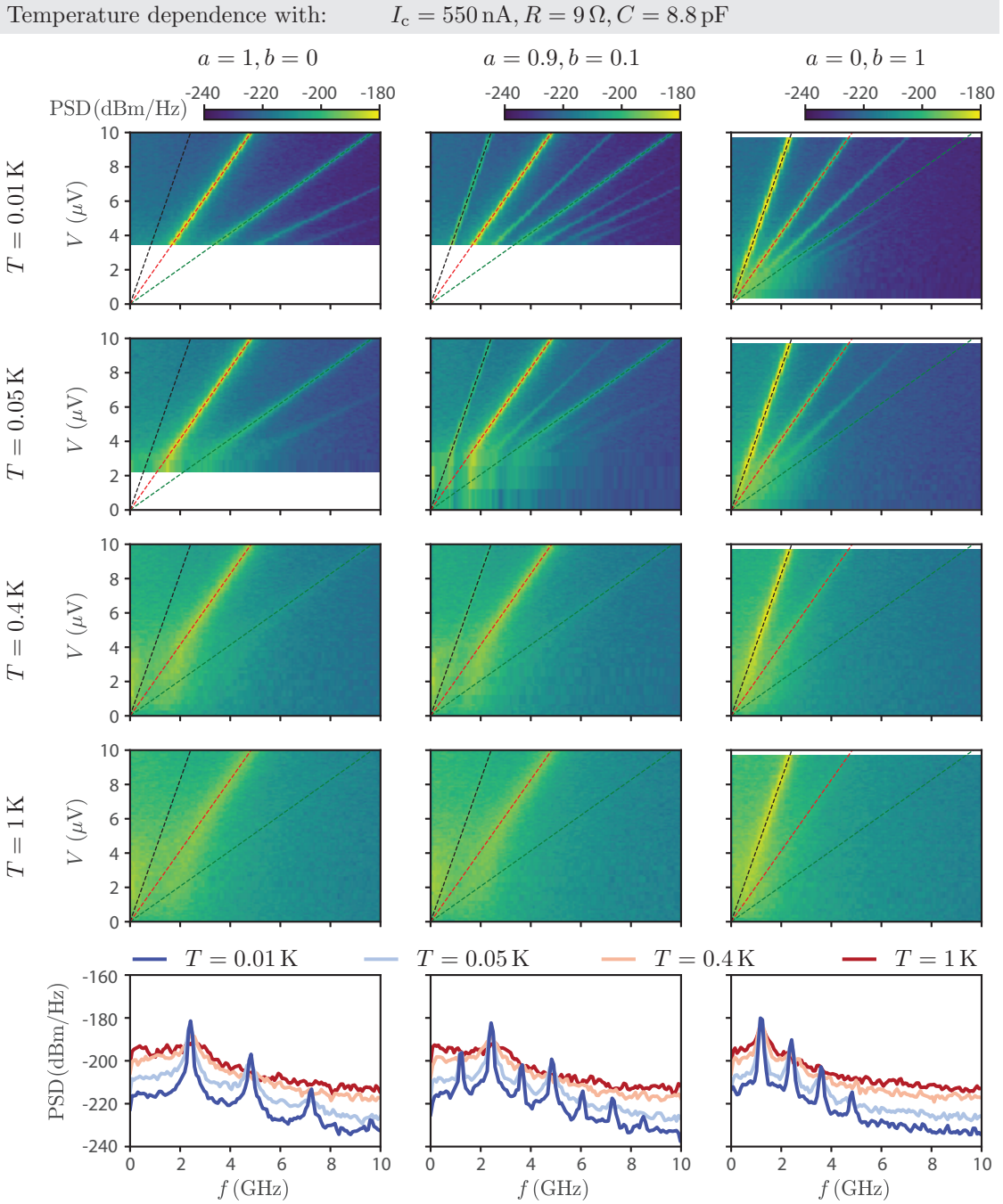
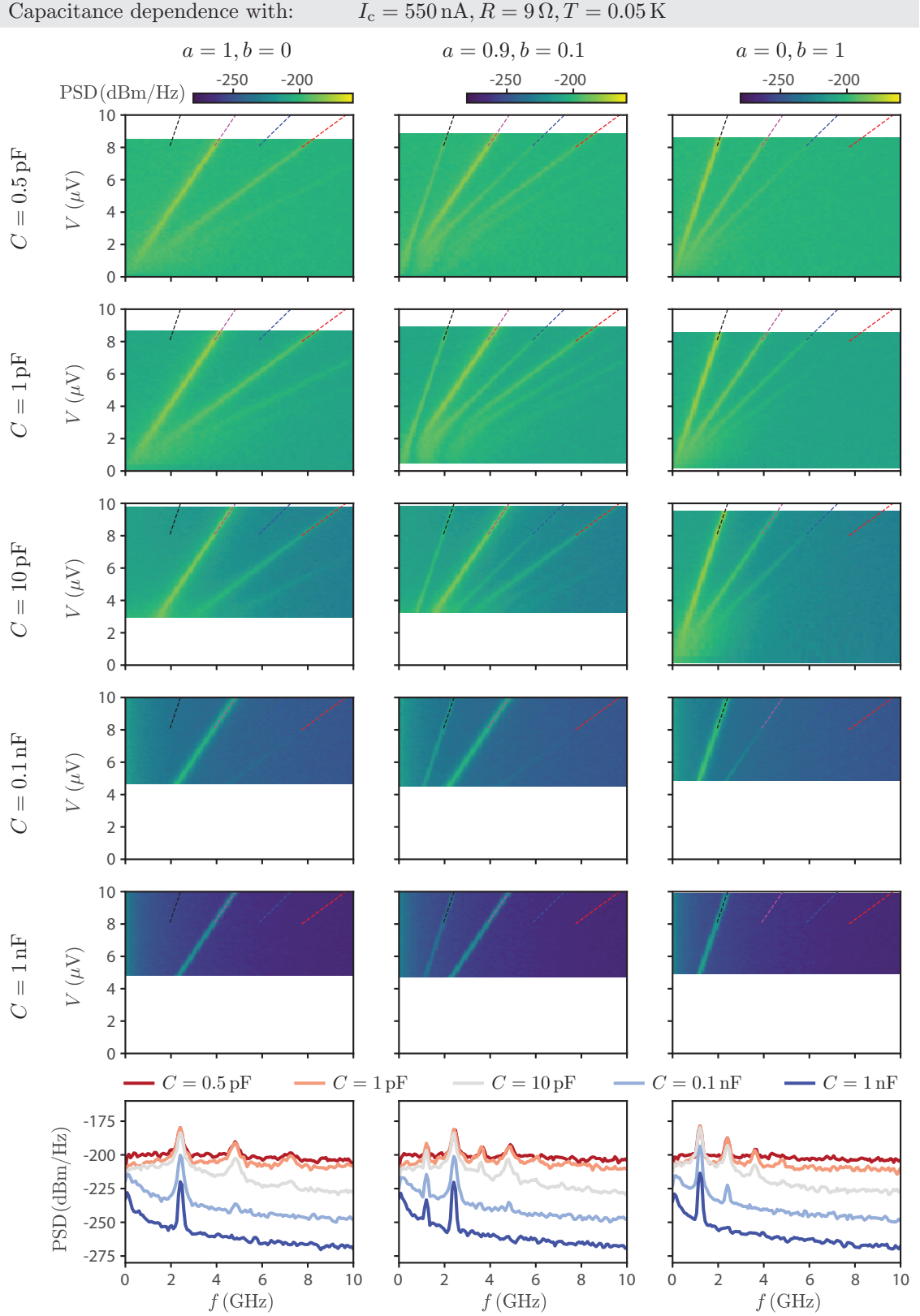


FIG. S1. Simulated Josephson radiation as a function of effective electronic temperature T for different combinations of trivial (a) and topological (b) supercurrent contributions in the current-phase relation for the circuit parameters given in the header. Radiation maps: Power spectral density (PSD) as a function of mean voltage V and frequency f . The bottom row shows cuts through the different maps at $V = 5 \mu\text{V}$. Guides for the eye: topological feature $V = hf/e$ (black dashed), trivial feature $V = hf/(2e)$ (red dashed), higher-order feature $V = hf/(4e)$ (green dashed).



SII. FABRICATION

Cd_3As_2 nanowires were grown by K. Park with the vapor transport method [S6–S11]. The nanowires are transferred from the growth batch with a cleanroom wipe snippet onto a highly p -doped Si/SiO_2 ($500\text{ }\mu\text{m}/305\text{ nm}$) wafer with pre-patterned Au markers and bonding pads. After removing the native oxide of the nanowires with Ar-milling, the wire is in-situ contacted by Ti/Al ($3\text{ nm}/200\text{ nm}$) electrodes in a quasi-four-probe configuration as seen in Fig. 1(a), in the main text. The wire has a diameter of 50 nm and the junction length is 150 nm . The Al leads extend from the nanowire up to the inner border of the base structures. We cover this inner region, indicated by the green box in Fig. 1(c) in the main text, with a 20 nm thick locally deposited HfO_2 gate-dielectric. A subsequently deposited Au top gate allows tuning of the charge carrier density.

SIII. MEASUREMENT SETUP

Both Josephson radiation and Shapiro step measurements are performed in a Triton 200 dilution refrigerator, of which the experimental setup is similar to Ref. [S12].

We start our description with the PCB shown in Fig. S3(a) that hosts co-planar transmission lines with SMP connectors and dc lines connecting to a nano-D adapter. The in-house designed double-sided Ni/Au plated Rogers[®] 4350 PCB is mounted onto a copper plate. A $10\text{ }\Omega$ metal film resistor is soldered on the back side of the PCB in between the ground plane and the central conductor of the SMP connector. The hole in the PCB exposes the bare copper backplate to which we mount the sample close to the co-planar transmission line. The SMP central conductor is bonded to one side of the junction, whereas the other side is bonded to the PCB ground resulting in a resistively shunted junction configuration. Both wire bonds are made as short as possible. Additional bond wires connect to the differential voltage measure and gate voltage supplies (not shown).

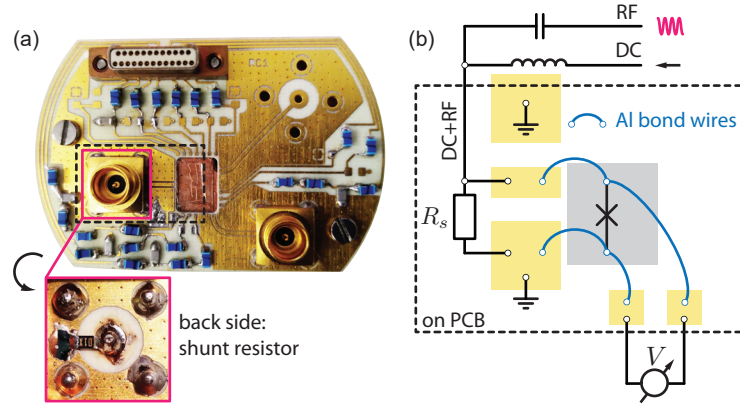


FIG. S3. PCB for Josephson radiation and Shapiro step measurements. (a) Optical image of the PCB with a length of 4 cm and width of 2.5 cm . The metal film shunt resistor ($R_s = 10\text{ }\Omega$ from Welwyn: PCD0603R-10RBT1) is soldered between the central pin and the ground plane on the back side of the rf SMP connector. (b) Representation of the bonding scheme to link the Josephson junction device to the measurement setup.

After inserting the PCB, the device connects to the full measurement setup presented in Fig. S4. The dc supply lines are filtered at room temperature, on the PCB, and are thermalized to the mixing chamber plate via silver-epoxy filters that provide a cut-off of $\sim 6\text{ MHz}$ [S13, S14]. We use home-built LC - π -filters ($L = 10\text{ }\mu\text{H}$, $C = 100\text{ nF}$) to minimize the noise on the dc supply for the HEMT amplifier [S15]. The Fisher cable connecting the break-out box to the cryostat looms and the cable connecting the 4 K HEMT amplifier with its power supply are surrounded by several ferrites. The break-out box shield is linked to the cryostat ground with a massive copper mesh cable, which is kept as short as possible (indicated with the red line). A current bias is generated by a $1\text{ M}\Omega$ resistor in series with a voltage source. The current couples via a bias-tee to the rf line that connects through the device to ground. The differential voltage drop across the junction is measured with a voltage amplifier and lock-in techniques. In the superconducting regime, most of the current flows through the junction, and once the junction switches to the normal state, most of the current will flow through the shunt resistor where the exact current division depends on the ratio between the junction normal state resistance R_N and the shunt resistance R_s . Since $R_N \gg R_s$ as discussed in Sec. SV, the $1\text{ M}\Omega$ source and the $10\text{ }\Omega$ shunt resistor act as a voltage divider and provide a stable voltage drop across the junction.

The radiation generated by the junction is amplified using a cryogenic HEMT amplifier at the 4 K stage, a room temperature amplifier, and finally measured with a spectrum analyzer. Two circulators at the HEMT input limit back-action noise, but limit the detection bandwidth to 2.5 – 3.8 GHz. The following parameters on the spectrum analyzer were used: detection bandwidth 20 MHz, span 24 MHz, radio bandwidth 10 MHz, video bandwidth 5 MHz and 1001 points resulting in a sweep time of 2 s over the detection frequency range. In addition to the sensing line, a drive line links to the device via a directional coupler used for irradiating the junction with a signal generator in Shapiro step measurements.

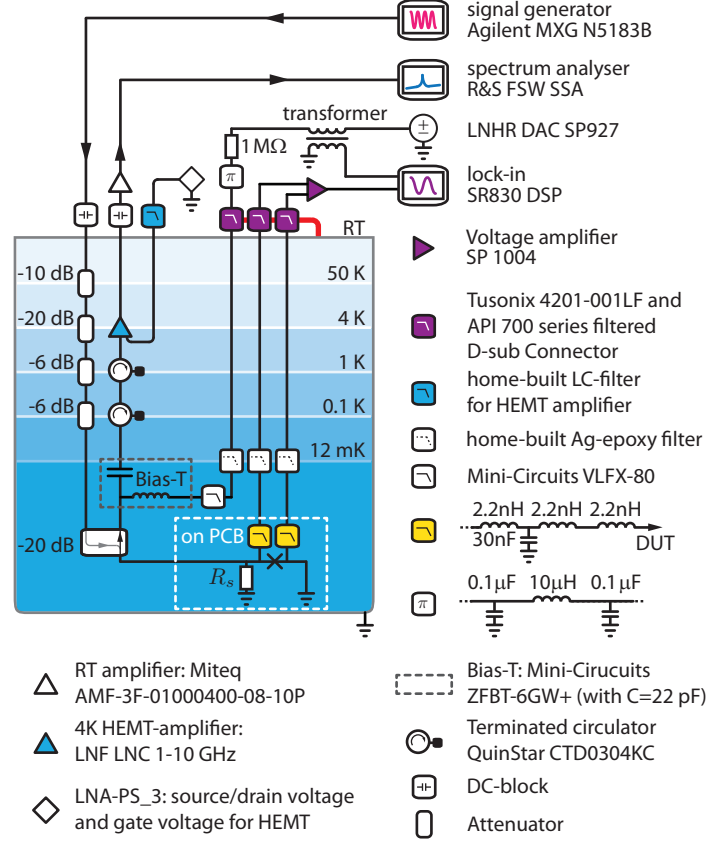


FIG. S4. Detailed overview of a hybrid Josephson radiation and Shapiro step measurement setup.

SIV. JOSEPHSON EMISSION POWER

Comparison of power levels in the experiment and simulation

In this section, we discuss the difference in absolute power level between experiment and simulation. For this purpose, we calculate the total radiation power P by integrating the spectral density of the conventional radiation peak defined with the relation $V = (h/2e)f$, for different values of the critical current. The experimental relation $P_{\text{det}}(I_c^2)$ is fitted with a line going through the origin, and results in a slope of $s_{\text{exp}}^V = 1.425 \times 10^4 \Omega$ as shown in gray dashed in Fig.3 in the main text. The simulation allows us to carry out the integration of the peak power over frequency and voltage as well, and the subsequent linear fit results in $s_{\text{sim}}^V = 0.227 \Omega$ for the integration over voltage (red dashed), and $s_{\text{sim}}^f = 0.205 \Omega$ for the integration over frequency (blue dashed) as shown in Fig.5 in the main text. To be consistent with the evaluation of the experimental data, we calculate in the following with s_{sim}^V . In the main text, we evaluated the modeled radiation power with $P = V_{\text{rms}}^2/|Z_L|$, by assuming the junction to be an ideal voltage source. However, taking into account a finite output impedance Z_s as illustrated in the circuit shown in Fig.S5(b), the power dissipated in the load Z_L is $P_L = V_{\text{rms}}^2|Z_L|/|Z_s + Z_L|^2$. This yields a correction factor of $t_P = P_L/P = |Z_L/(Z_L + Z_s)|^2$. We model the junction source impedance with the shunt resistor R in parallel with the shunt capacitor C as shown in Fig.S5(a), resulting in $Z_s = RZ_c/(R + Z_c)$, where $Z_c = 1/(i2\pi fC)$. The load impedance is set to $Z_L = 50 \Omega$ according to the input impedance of the spectrum analyzer. At $f = 3 \text{ GHz}$, with $C = 8.8 \text{ pF}$ and $R = 9 \Omega$, we get $t_P \approx 0.83$. The ratio $s_{\text{exp}}^V/(t_P s_{\text{sim}}^V)$ evaluates the power translation between the experiment and the simulation, which reads in dB-scale:

$$g_{\text{exp}} = 10 \cdot \log_{10} (s_{\text{exp}}^V/(t_P s_{\text{sim}}^V)) = 48.8 \text{ dB}. \quad (\text{S21})$$

Next, we compare this amplification to the gain of the amplification chain present in the experimental setup (see Fig.S4). By considering the gain of the HEMT amplifier (+27 dB) and the room-temperature amplifier (+39 dB), as well as the attenuation of the measurement line (−13 dB), we estimate a total effective gain of

$$g_{\text{eff}} \approx 51 \text{ dB}, \quad (\text{S22})$$

which gives us a reasonable agreement between the power level in the experiment and the simulation. After the experiment has been conducted, it turned out that the supply lines to the HEMT-amplifier were high-ohmic, such that its ideal working point with the highest gain (nominally +40 dB) and lowest thermal noise could not be reached. The small discrepancy between g_{eff} and g_{exp} can be attributed to uncertainties in the experimental setup.

Interpretation of the $P(I_c^2)$ -relation

We explain the quadratic dependence between P_{det} and I_c as follows. We model the junction as a sinusoidal current source, with a current amplitude I_c and source impedance Z_s as illustrated in Fig.S5(c). Here, Z_s is as well R in parallel with C . Since $I_{\text{rms}} = I_c/\sqrt{2}$, the power transferred to the load Z_L is

$$P_L = \frac{1}{2} \left| \frac{Z_s}{Z_s + Z_L} \right|^2 |Z_L| \cdot I_c^2. \quad (\text{S23})$$

With $C = 8.8 \text{ pF}$, $R = 9 \Omega$ and $Z_L = 50 \Omega$, we obtain at $f = 3 \text{ GHz}$, $P_L \approx 0.224 \Omega \cdot I_c^2$, which resembles the $P(I_c^2)$ -relation extracted from the model. In the experimental configuration, the transferred power is amplified with a gain of g , and the detected power is $P_{\text{det}} = gP_L = \mathcal{R}I_c^2/2$. We note that formula S23 should be considered when designing experiments. For a high power transfer, $Z_s \gg Z_L$ is preferred, however, for stable biasing in the finite detection window, the junction should not be in the hysteretic regime. The trade-off between the sufficient damping of the junction and the optimization of the power transfer could be balanced with an in-situ variable shunt resistance.

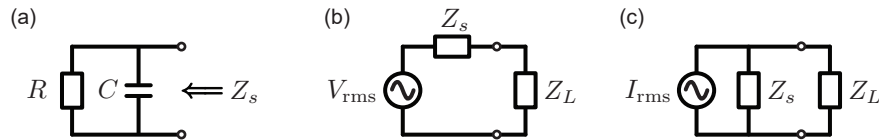


FIG. S5. (a) Impedance Z_s of a parallel RC -circuit modeling the source impedance of the Josephson junction. (b) AC voltage source with root-mean-square voltage V_{rms} and impedance Z_s connected to a load impedance Z_L . (c) AC current source with root-mean-square current I_{rms} and impedance Z_s connected to a load impedance Z_L .

SV. $I_c R_N$ PRODUCT

We obtained the normal state resistance R_N from measurements carried out in a magnetic field of 20 mT, above the critical field of the junction. We use a 100 nA ac excitation on the lock-in amplifier and correct for the parallel shunt resistor R_s . In Fig. S6(a) we initially observe the expected inverse correlation between I_c and R_N . However, when looking at the $I_c R_N$ product in Fig. S6(b), we observe an $I_c R_N \sim 50 \mu\text{V}$ in the far negatively doped regime up to $\sim 100 \mu\text{V}$ where I_c is at its maximum value. For more positive doping $I_c R_N$ again decreases with increasing R_N . Both the peak in I_c and $I_c R_N$ close to $V_{\text{tg}} = -2 \text{ V}$ (i.e., the Dirac point), hint towards supercurrent carried by the surface states, and an increase of bulk-surface interaction when the doping level is increased away from the Dirac point [S9].

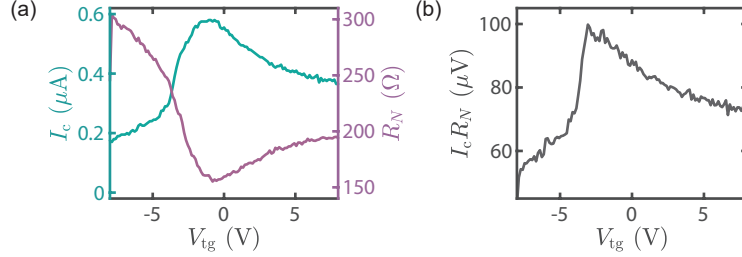


FIG. S6. Gate dependent critical current I_c and normal state resistance R_N . (a) Left axis (green) I_c and right axis (violet) R_N as a function of gate voltage V_{tg} . (b) $I_c R_N$ -product as a function of V_{tg} .

SVI. SHAPIRO STEPS EVALUATION

In this section, we compare simulated Shapiro step patterns with measurement data, and use parameters that describe the modification of the pattern due to the presence of a topological supercurrent. In a conventional Josephson junction with a 2π -periodic CPR, steps at the Shapiro voltages $V_k = k \frac{\hbar}{2e} f_d$ appear. Here, f_d is the drive frequency and k is an integer that represents the number of 2π phase evolutions that the particle undergoes in the tilted washboard potential. For topological supercurrents, a 4π -periodic CPR results in a 4π phase evolution and thus results in Shapiro voltages of height $V_k = k \frac{\hbar}{e} f_d$, double compared to the trivial Shapiro voltage. In Shapiro step patterns, the presence of topological supercurrent therefore effectively suppresses the relative current magnitude associated with odd steps with 2π supercurrent periodicity, in favor of the even current steps which entail both 2π and 4π contributions [S16].

Fig. S7, left column, shows simulated data of Shapiro steps as a function of the microwave power P_d and current bias I , while the middle column shows the accompanying dc current plateau widths for which the constant Shapiro voltages appear. Starting from a pure conventional current ($a = 1 - b = 1$, $b = 0$), an increased ratio of conventional to topological current (see a and b values) is plotted when moving down vertically. The maximum step width is quantified by the lobe maxima (colored crosses) and we show a reduction of the step width for odd k for increasing b , which is a direct consequence of the different admixture of 2π and 4π CPR components. The odd steps ($n = 1, 3$) almost vanish when only topological current is present ($a = 0$, $b = 1$), but a small step due to higher order modes remains. We quantify the change in the even to odd ratios by introducing the relative plateau width parameter $Q_{nm} = I_{\text{max},n}/I_{\text{max},m}$, defined as the ratio between the maximal current plateau width $I_{\text{max},n}$ of step n , divided by the current plateau width of $I_{\text{max},m}$ of $m = n + 1$. These ratios are plotted for the first three lobes.

The Q_{12} and Q_{23} ratios for the conventional case ($a = 1$, $b = 0$), are monotonically decreasing for each successive lobe, while Q_{12} is always larger than Q_{23} . Comparing this case $a = 0.95$ and $b = 0.05$, the small fraction of topological current moves Q_{12} and Q_{23} value closer together (the second lobe values almost overlap), indicating that the odd $n = 1$ step decreases in relative magnitude. For $b = 0.2$, Q_{12} is smaller than Q_{23} for all lobes, a trend that continues until for $b = 1$, the $n = 1$ step almost completely disappears, reflected by the high value of Q_{23} .

We now compare our results from the simulation with experimental results shown in Fig. S9. Again, the left column shows Shapiro steps as a function of P_s and I , the middle column shows the extracted step heights in I , while the right column shows the associated Q_{12} and Q_{23} values. From top to bottom, we move from hole doping at $V_{\text{tg}} = -5 \text{ V}$, to close to the Dirac point at $V_{\text{tg}} = 0 \text{ V}$, and finally to electron doping at $V_{\text{tg}} = 7 \text{ V}$. Although small changes in the absolute and relative Q_{12} and Q_{23} can be distinguished, no clear evidence of suppression of the first $n = 1$ step can be observed. An important note is that the junction parameters used in the simulations in Fig. S9 are fitted to match the measurement data for $V_{\text{bg}} = 0 \text{ V}$. The lower I_c for $V_{\text{bg}} = -5 \text{ V}$ and $V_{\text{bg}} = 7 \text{ V}$ changes the dynamics of the junction

which, in turn, modifies the plateau widths and the Q_{12} and Q_{23} values, on top of any potential modification due to a topological supercurrent contribution. To establish signatures of topological supercurrent, one therefore desires to measure Shapiro patterns over a wide frequency range, while keeping the junction parameters constant [S16, S17].

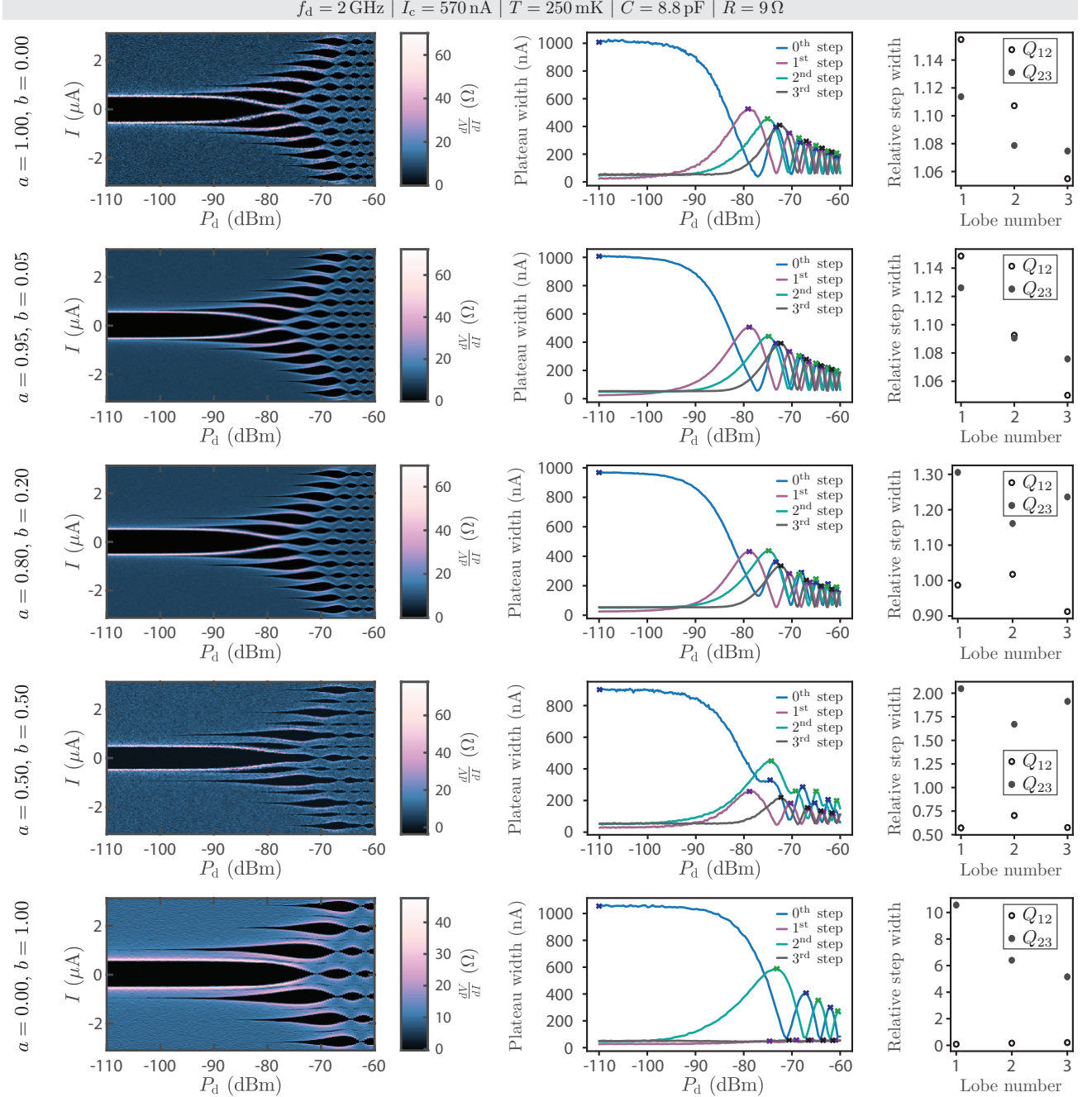


FIG. S7. Simulated Shapiro patterns and current plateau widths for various trivial (a) and topological (b) supercurrent contributions. Circuit parameters used for the circuit parameters are given in the header. Left column: Shapiro maps showing differential resistance dV/dI as a function of drive power P_d and current bias I . Middle column: Evolution of the plateau widths as a function of drive power P_d , corresponding to the left column for the first four steps. The maxima of the plateaus are indicated with crosses. Right column: Relative step widths for the first three lobes. Q_{nm} describes the ratio between the maximal current plateau widths of step n divided by the ones of $m = n + 1$.

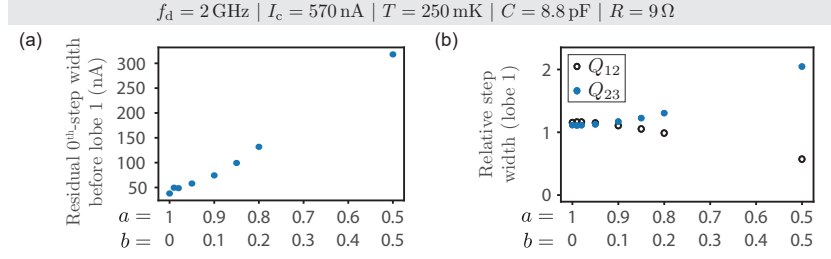


FIG. S8. Simulated topological indicators when sweeping the a to b ratio for the circuit parameters given in the header. (a) Minimum of the current plateau width between the first and second lobe for the 0th-step (blue). (b) Relative step widths for the first lobes. Q_{nm} describes the ratio between the maximal current plateau widths of step n divided by the ones of $m = n + 1$.

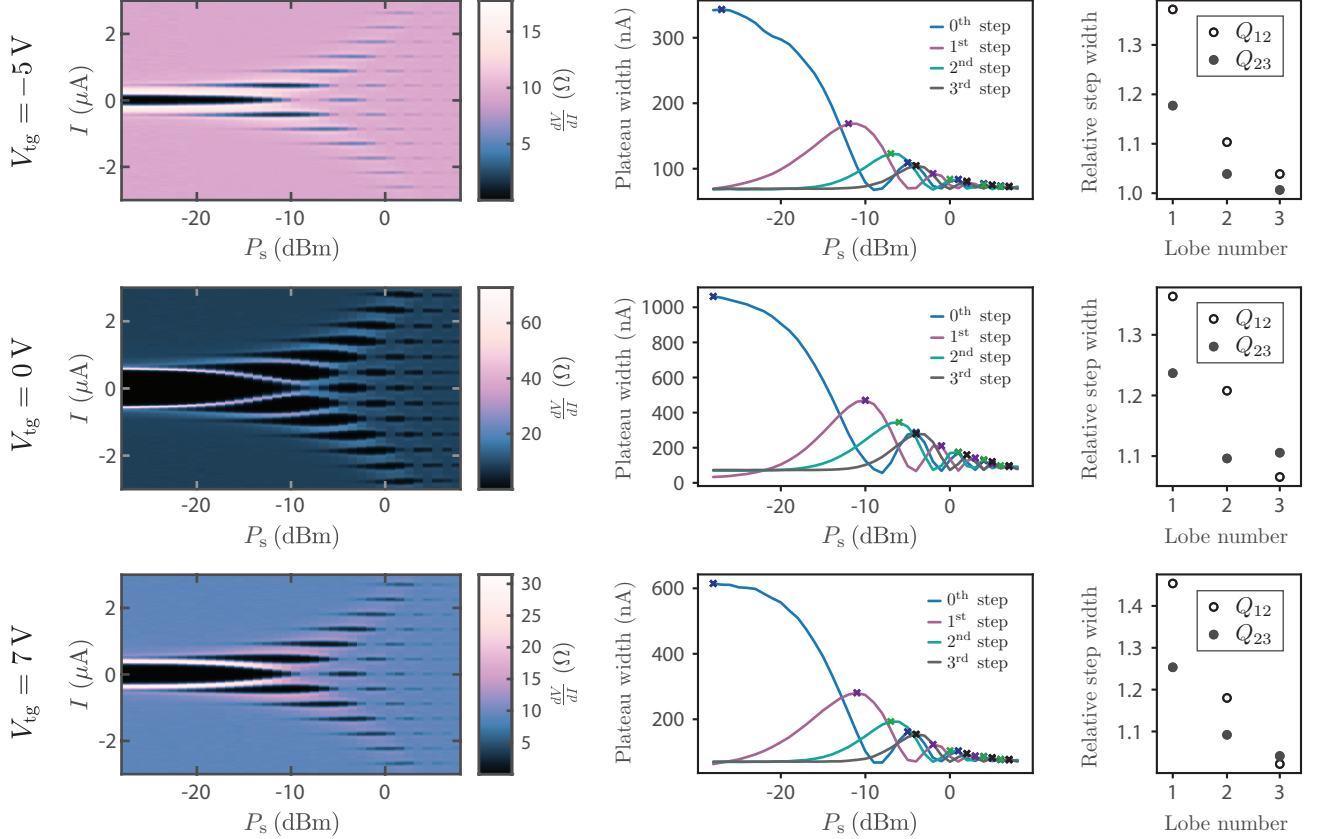


FIG. S9. Measured Shapiro patterns with drive frequency $f_d = 2 \text{ GHz}$ and current plateau widths for three gate voltages. Left column: Shapiro maps showing differential resistance dV/dI as a function of drive power P_s at the microwave source and current bias I . Middle column: Evolution of the plateau widths as a function of drive power P_s , corresponding to the left column for the first four steps. The maxima of the plateaus are indicated with crosses. Right column: Relative step widths for the first three lobes. Q_{nm} describes the ratio between the maximal current plateau widths of step n divided by the ones of $m = n + 1$.

We additionally perform a simulated parameter sweep of Q_{12} and Q_{23} for the first lobe as a function of a and b in Fig. S8(b). The same trend is observed: for an increasing topological current contribution, Q_{12} increases while Q_{23} decreases. Although this trend is visible even for small topological current fractions of $b \sim 0.05$, the crossing point where $Q_{12} = Q_{23}$ at $b \sim 0.1$ can be used as a clear indicator in an experiment for a topological supercurrent contribution. Finally, we look at another indicator for a topological current contribution shown in Fig. S8(a), namely the minimum, e.g., depression of the current plateau width between the first and second lobe of the 0th step [S18]. This supplementary indicator is a stronger function for increasing b than the Q parameters, which might give indications for even smaller topological supercurrents. However, more in-depth research is required to investigate this indicator as a function of the junction parameters. The scripts used to perform the Shapiro step width analysis and the generation of the plots can be found in Ref. [S19].

-
- [S1] Python code of the RCSJ model is available on https://github.com/donfuge/rcsj_sde.
- [S2] R. L. Kautz and J. M. Martinis, Noise-affected I - V curves in small hysteretic Josephson junctions, *Phys. Rev. B* **42**, 9903 (1990).
- [S3] R. Gross, A. Marx, and F. Deppe, *Applied superconductivity: Josephson effect and superconducting electronics* (De Gruyter, 2016).
- [S4] W. Rümelin, Numerical Treatment of Stochastic Differential Equations, *SIAM Journal on Numerical Analysis* **19**, 604 (1982).
- [S5] P. Welch, The use of fast Fourier transform for the estimation of power spectra: A method based on time averaging over short, modified periodograms, *IEEE Transactions on Audio and Electroacoustics* **15**, 70 (1967).
- [S6] M. Jung, K. Yoshida, K. Park, X.-X. Zhang, C. Yesilyurt, Z. B. Siu, M. B. A. Jalil, J. Park, J. Park, N. Nagaosa, J. Seo, and K. Hirakawa, Quantum Dots Formed in Three-dimensional Dirac Semimetal Cd_3As_2 Nanowires, *Nano Letters* **18**, 1863 (2018).
- [S7] S. Jeon, B. B. Zhou, A. Gyenis, B. E. Feldman, I. Kimchi, A. C. Potter, Q. D. Gibson, R. J. Cava, A. Vishwanath, and A. Yazdani, Landau quantization and quasiparticle interference in the three-dimensional Dirac semimetal Cd_3As_2 , *Nat. Mater.* **13**, 851 (2014).
- [S8] K. Park, M. Jung, D. Kim, J. R. Bayogan, J. H. Lee, S. J. An, J. Seo, J. Seo, J.-P. Ahn, and J. Park, Phase Controlled Growth of Cd_3As_2 Nanowires and Their Negative Photoconductivity, *Nano Letters* **20**, 4939 (2020).
- [S9] C. Z. Li, C. Li, L. X. Wang, S. Wang, Z. M. Liao, A. Brinkman, and D. P. Yu, Bulk and surface states carried supercurrent in ballistic Nb-Dirac semimetal Cd_3As_2 nanowire-Nb junctions, *Phys. Rev. B* **97**, 115446 (2018).
- [S10] C.-Z. Li, L.-X. Wang, H. Liu, J. Wang, Z.-M. Liao, and D.-P. Yu, Giant negative magnetoresistance induced by the chiral anomaly in individual Cd_3As_2 nanowires, *Nature communications* **6**, 10137 (2015).
- [S11] E. Zhang, Y. Liu, W. Wang, C. Zhang, P. Zhou, Z.-G. Chen, J. Zou, and F. Xiu, Magnetotransport Properties of Cd_3As_2 Nanostructures, *ACS Nano* **9**, 8843 (2015).
- [S12] R. S. Deacon, J. Wiedenmann, E. Bocquillon, F. Domínguez, T. M. Klapwijk, P. Leubner, C. Brüne, E. M. Hankiewicz, S. Tarucha, K. Ishibashi, H. Buhmann, and L. W. Molenkamp, Josephson Radiation from Gapless Andreev Bound States in HgTe-Based Topological Junctions, *Phys. Rev. X* **7**, 021011 (2017).
- [S13] T. Hasler, *Microwave noise detection of a quantum dot with stub impedance matching*, Ph.D. thesis, University of Basel (2016).
- [S14] C. P. Scheller, S. Heizmann, K. Bedner, D. Giss, M. Meschke, D. M. Zumbühl, J. D. Zimmerman, and A. C. Gossard, Silver-epoxy microwave filters and thermalizers for millikelvin experiments, *Applied physics letters* **104**, 211106 (2014).
- [S15] R. Haller, *Probing the microwave response of novel Josephson elements*, Ph.D. thesis, University of Basel (2021).
- [S16] J. Park, Y.-B. Choi, G.-H. Lee, and H.-J. Lee, Characterization of Shapiro steps in the presence of a 4π -periodic Josephson current, *Phys. Rev. B* **103**, 235428 (2021).
- [S17] Y. Jang and Y.-J. Doh, Optimal conditions for observing fractional Josephson effect in topological Josephson junctions, *J. Korean Phys. Soc.* **78**, 58 (2021).
- [S18] A.-Q. Wang, C.-Z. Li, C. Li, Z.-M. Liao, A. Brinkman, and D.-P. Yu, 4π -Periodic Supercurrent from Surface States in Cd_3As_2 Nanowire-Based Josephson Junctions, *Phys. Rev. Lett.* **121**, 237701 (2018).
- [S19] See the Python script in folder 'shapiro_evaluation' in the Zenodo repository 10.5281/zenodo.7961884 to extract the current plateau widths from Shapiro maps.